Chemical Geology 696 (2025) 123093

Contents lists available at ScienceDirect

Chemical Geology

journal homepage: www.elsevier.com/locate/chemgeo

Tectonic thickening in stagnant to mobile lid transition facilitated the stabilization of Archean cratons

Ning Ding [a], Chris Hawkesworth [b], Xiao-Lei Wang [a,*], Rong-Feng Ge [a], Axel Hofmann [c], Jun-Yong Li [a]

[a] State Key Laboratory for Critical Earth Material Cycling and Mineral Deposits, School of Earth Sciences and Engineering, Frontiers Science Center for Critical Earth Material Cycling, Nanjing University, Nanjing 210023, China
[b] Department of Earth Sciences, University of Bristol, Bristol BS8 1RJ, UK
[c] Department of Geology, University of Johannesburg, Johannesburg 2006, South Africa

ARTICLE INFO

Editor: Marco Fiorentini

Keywords:
Archean cratons
Zircon
Oxygen fugacity
Subduction

ABSTRACT

Archean cratons are the oldest domains of tectonically stable continental crust and their formation coincided with the widespread emplacement of potassic granites, which reflects reorganization of crustal composition. However, the factors influencing the shifts in crustal composition and craton stability remain controversial. In this study of ca. 3.51–3.22 Ga trondhjemite-tonalite-granodiorite (TTG) and ca. 3.11–3.10 Ga potassic granites of the eastern Kaapvaal craton, we apply a newly developed zircon oxybarometer-hygrometer and document a progressive increase of magmatic fO_2 values and H_2O contents from ca. 3.51 to 3.22 Ga, peaking at ca. 3.10 Ga with values higher than those of known Archean granitic rocks and similar to modern orogenic granites. Concurrent increases in magma crystallization depths and crustal thickness culminated at 3.11–3.10 Ga. These trends reflect a tectonic transition from stagnant lid (3.66–3.23 Ga) to mobile lid (3.22–3.10 Ga) in eastern Kaapvaal craton, supported by isotopic shifts from juvenile to evolved Hf-O signatures. The combination of thermodynamic and geochemical modeling demonstrates that the widespread ca. 3.11–3.10 Ga potassic granites originated from partial melting of the middle to lower crust in regions of crustal thickening. The Kaapvaal Craton is proposed to be among the earliest cratons that witnessed tectonic thickening in stagnant to mobile lid transition, which might have played a critical role in the earliest stabilization and maturation of cratons.

1. Introduction

Cratons represent the oldest and most stable geological units on Earth. They preserve vital clues about the formation and evolution of early felsic crust and offer invaluable insights into our planet's early history (De Wit et al., 1992; Hawkesworth et al., 2017). These stable units typically have substantial roots, comprising thickened crust and an underlying cold, dry, and residue-rich lithosphere (Griffin et al., 2003; Pearson et al., 2021; Cawood et al., 2022). The cratonic middle and upper crust is composed of granitoids and greenstones, with the former comprising predominantly sodium-rich trondhjemite-tonalite-granodiorite (TTG) with less potassic granites (Laurent et al., 2014). TTGs are thought to have formed through partial melting of hydrated mafic crust to form sodium-rich TTG magmas (Smithies, 2000; Martin et al., 2005; Moyen and Martin, 2012). In contrast, the potassic granites appear to have been derived from the reworking of felsic crust or mafic protocrust (Næraa et al., 2014; Moyen et al., 2021; Rollinson et al., 2024). Globally, a significant and abrupt shift of felsic magmatism within cratons is observed in many cratons, with the composition transitioning from sodium-rich TTG suites to potassium-rich magmatic rocks (Keller and Schoene, 2012; Laurent et al., 2014; Cawood et al., 2022). This compositional transition is widely regarded as concomitant with the stabilization of Archean cratons, although the exact timing of this stabilization varied between different cratons (Dhuime et al., 2015; Cawood et al., 2022). Nonetheless, the mechanism that drives the change of granitic magmatism and whether it corresponds to a shift in tectonic settings remains unclear.

Extensive occurrences of potassium-rich magmatic events linked to cratonization have been documented at around 3.10 Ga in the eastern Kaapvaal craton and Singhbhum craton (Robb et al., 2021; Hofmann et al., 2022). While sporadic occurrences of older (>3.5 Ga) potassic granites exist as clasts within younger strata (Sanchez-Garrido et al.,

* Corresponding author.
E-mail address: wxl@nju.edu.cn (X.-L. Wang).

https://doi.org/10.1016/j.chemgeo.2025.123093
Received 3 June 2025; Received in revised form 26 September 2025; Accepted 12 October 2025
Available online 13 October 2025
0009-2541/© 2025 Elsevier B.V. All rights are reserved, including those for text and data mining, AI training, and similar technologies.

2011; Kröner et al., 2018), their presence does not necessarily signify cratonization. Instead, they are more likely products of magmatic evolution or localized reworking of early felsic rocks (Ding et al., 2024). Situated in the eastern part of the Kaapvaal craton, the Barberton granitoid-greenstone terrain (BGGT) in South Africa and the adjacent deeper crustal equivalent, the Ancient Gneiss Complex (AGC) in Eswatini, document a chronological sequence of rocks spanning from the Paleoarchean to the Mesoarchean (Kröner and Hofmann, 2019; Moyen et al., 2019). This encompasses ca. 3.66–3.22 Ga TTGs and their gneissic equivalents and ca. 3.11–3.10 Ga potassic granites. The tectonic settings that operated in this area are highly debated, including ca. 3.66–3.20 Ga long-lived oceanic plateau/stagnant lid (André et al., 2022; Lowe, 2024) and ca. 3.30–3.22 Ga subduction models (Schoene et al., 2009; Wang et al., 2022). Furthermore, the mechanism of transition from ca. 3.51–3.22 Ga long-term episodic TTG magmatic events toward ca. 3.11–3.10 Ga short-term potassic granitoids remains a matter of discussion (Laurent et al., 2014; Robb et al., 2021; Moyen et al., 2021). These granitoids in BGGT and AGC therefore provide a critical window to understand the tectonic processes and their relationship with craton stabilization.

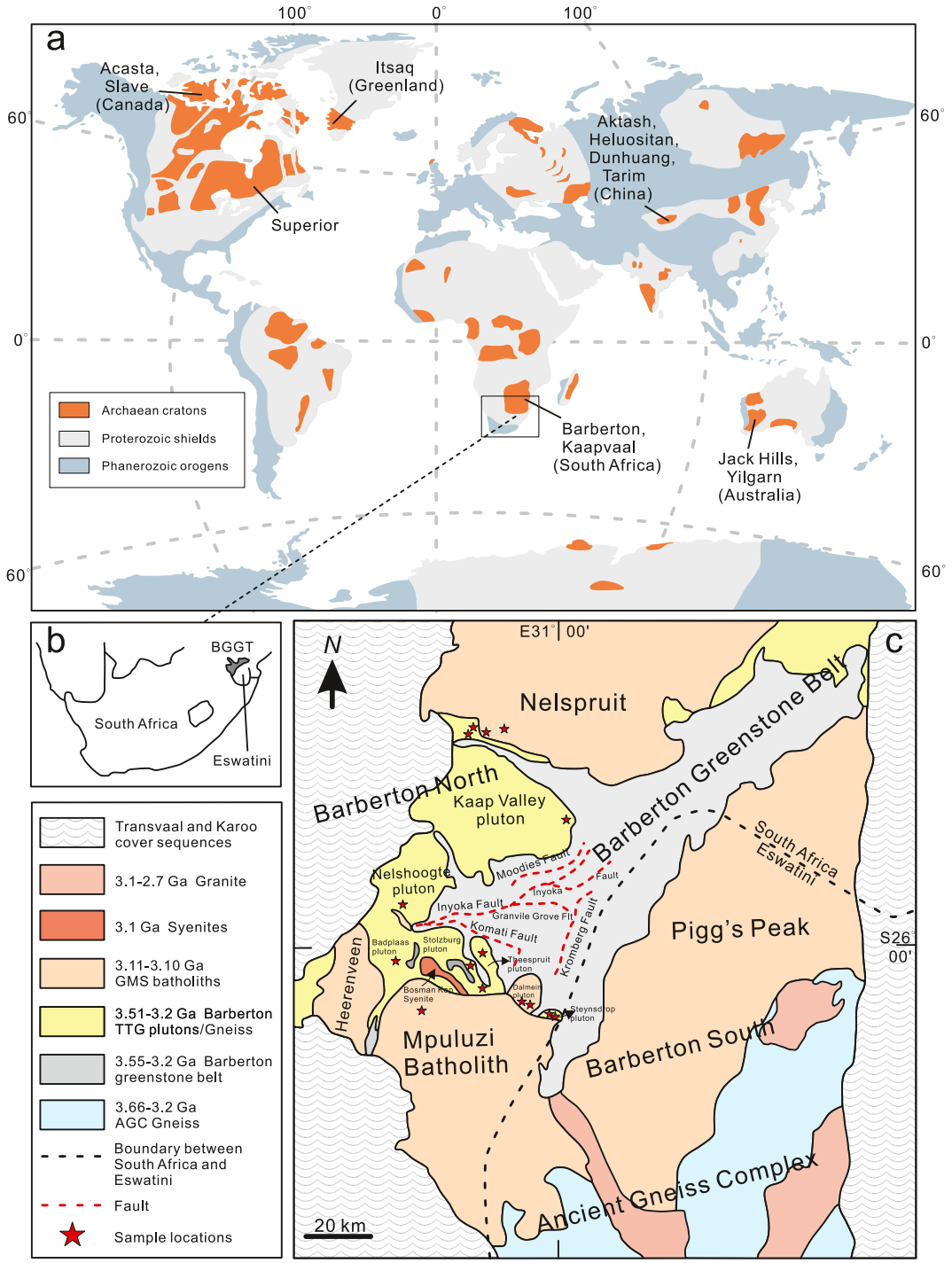

Fig. 1. (a) Distribution of Archean cratons, Proterozoic shields and Phanerozoic orogens in the world (modified from Furnes et al., 2015). The locations of Archean rocks discussed in this manuscript was labeled. (b) Simplified geographical locations of South Africa, Eswatini and Barberton granitoid-greenstone terrain (BGGT). (c) Simplified geological map of the BGGT and part of Ancient Gneiss Complex (AGC) in Eswatini (modified from Moyen et al., 2021; Byerly et al., 2019).

Granites formed in different tectonic settings vary in oxygen fugacity, water content, and isotopic signatures. Specifically, subduction zone granites typically exhibit higher oxygen fugacity, water content, and oxygen isotope values than those from intraplate environments (Cottrell et al., 2021; Ge et al., 2023). In this study, we investigate the geochemical proxies of zircon and document that the magmatic fO_2 and H_2O content increased from ca. 3.51–3.22 Ga TTG to ca. 3.11–3.10 Ga potassic granites, at values higher than those of other known Archean granitic rocks and similar to modern orogenic granites and collision-type porphyry deposits. We argue that the increased magmatic fO_2 and H_2O reflects a change in tectonic setting in the eastern Kaapvaal craton at ca. 3.23–3.10 Ga, and that this transition facilitated the stabilization and maturation of the craton. This model is further supported by the increase in crustal thickness and the shift from mainly juvenile to more evolved isotopic signatures from ca. 3.51 Ga to ca. 3.22–3.10 Ga. The formation of a stable and more oxidized continent at ca. 3.2–3.1 Ga in the eastern Kaapvaal craton is accompanied by intensified weathering and erosion, which likely drove changes in the surficial environment and influence the early ocean and atmosphere.

2. Geological background

The BGGT in South Africa and the neighboring AGC in Eswatini collectively form the eastern core of the Kaapvaal Craton, featuring rocks that were generated between ca. 3.66 and 3.10 Ga (Kamo and Davis, 1994; Kröner and Hofmann, 2019; Moyen et al., 2019; Fig. 1). Following widespread granite emplacement at ca. 3.11–3.10 Ga, the eastern Kaapvaal Craton stabilized as a continental block, largely untouched by later tectonic overprinting. This stability facilitated the formation of extensive intracontinental basins from ca. 3.00 to 2.06 Ga (Moser et al., 2001; Kröner and Hofmann, 2019). Prior to ca. 3.11 Ga, there was a series of continental growth and tectonic events, as evidenced by the Barberton Greenstone Belt (BGB), surrounding granitoid plutons, and AGC gneisses (Kisters and Anhaeusser, 1995; Kröner et al., 2014; Moyen et al., 2019).

The BGB consists of a suite of low-grade supracrustal rocks, starting with the mafic to ultramafic strata of the Onverwacht Group, dated between ca. 3.53 and 3.26 Ga (Armstrong et al., 1990; Byerly et al., 2019; Lowe, 2024). This is succeeded by the compositionally diverse Fig Tree Group (ca. 3.26 to 3.23 Ga), composed of intermediate to felsic volcanic rocks, together with clastic and chemical sediments. These are capped by the Moodies Group (ca. 3.23 to 3.21 Ga), featuring extensive strata of conglomerates and sandstones (Lowe, 2024). The Moodies Group unconformably overlies the older units, contains intraformational unconformities, and is deformed into tight, upright synclines, suggestive of *syn*-depositional tectonism (Byerly et al., 2019). The shift in sedimentary patterns, in conjunction with the belt's deformation, suggests a major tectonic episode (or episodes) during deposition of the Fig Tree and Moodies groups and its immediate aftermath (around 3.25 to 3.20 Ga). Coinciding with this timeframe is the amphibolite-facies metamorphism recorded in the nearby gneissic terrains (Dziggel et al., 2002; Cutts et al., 2014; Suhr et al., 2015). Surrounding the BGB, three main magmatic episodes gave rise to the formation of TTG plutons and gneissic equivalents older than 3.22 Ga (Fig. 1). These include the ca. 3.51 Ga Steynsdorp pluton; the ca. 3.45 Ga Stolzburg, Theespruit and related plutons; and the ca. 3.28 Ga (older phases of the Badplaas pluton) to ca. 3.22 Ga (younger phase of the Badplaas pluton, and the Nelshoogte and Kaap Valley plutons) TTGs (Moyen et al., 2019). To the south of the BGB, the AGC represents a segment of Archean middle to lower crust, mainly comprised of ca. 3.66–3.45 Ga multiply deformed granitoid gneisses, greenstone remnants and interlayered amphibolites, many of which are probably derived from mafic dykes (Hoffmann et al., 2016; Hoffmann and Kröner, 2019). In the center of the AGC, the Luboya-Kubuta terrane preserved ca. 3.11–3.07 Ga granulites at pressures of ~0.7 GPa and along clock-wise P-T paths, similar to those documented for metamorphism in modern collisional orogens (Taylor et al., 2012).

The ca. 3.11–3.10 Ga Granodiorite-Monzogranite-Syenite (GMS) suite consists of four main batholiths (Fig. 1): the Nelspruit batholith situated north of the BGB, the Pigg's Peak batholith located to the southeast within Eswatini, the Mpuluzi batholith to the south, and the Heerenveen batholith to the southwest (Robb et al., 2021; Moyen et al., 2021). The GMS batholiths are composite but dominantly granodiorite to monzogranite accompanied by smaller bodies of syenite to syenogranite, such as the Boesmanskop, Weergevonden and Kees Zyn Doorns intrusions emplaced at the same time as the larger batholiths (Kröner and Hofmann, 2019). Based on available geochronological data, the formation of the GMS suites can be constrained to a brief timespan, within the ca. 3.11 to 3.10 Ga interval (Moyen et al., 2019). Unlike the well-studied long-term episodic TTG magmatic events, the genesis of these short-term explosive potassic granitoids remains an enigma.

3. Methods

3.1. Phase equilibria and trace elements modeling

To conduct phase equilibria modeling, we used Perple_X (version 6.9.1) software package (https://www.perplex.ethz.ch/; Connolly, 2009) in the Na_2O-CaO-K_2O-FeO-MgO-Al_2O_3-SiO_2-H_2O-TiO_2-O_2 (NCKFMASHTO) chemical system, with the Holland and Powell (2011) (hp622ver.dat) thermodynamic database. Several mineral solid solution models were selected for crust melting, including tonalitic melt [Melt (HGP)], garnet [Gt(HGP)], biotite [Bi(HGP)], orthopyroxene [Opx (HGP)], amphibole [cAmph(G)], ilmenite [Ilm(WPH)], mica [Mica(W)], epidote [Ep(HP11)], and feldspar. The modeling was conducted at temperatures of 600–1000 °C and pressures of 0.3–1.8 GPa. The median composition of 3.55 Ga AGC gneiss (Kröner et al., 2014), Barberton TTGs, sedimentary rocks (shale, sandstone and greywacke of Fig Tree formation) was utilized as source of the 3.1 Ga GMS. We assumed the $Fe^{3+}/(Fe^{3+}+Fe^{2+})$ ratio of 0.1, in agreement with the general assumption that the Archaean surface environment was less oxygenated than modern environments of hydrothermal alteration for which $Fe^{3+}/(Fe^{3+}+Fe^{2+})$ ratio typically exceeds around 0.3 (Reimink and Smye, 2024). The initial water content was set at 4 wt%, considering the presence of a small amount of amphibole in ca. 3.2 Ga Barberton TTGs. We calculated mineral phase equilibria every 10 °C and 0.1 GPa from 600 to 1000 °C and 0.3–1.8 GPa for crustal rocks.

Based on phase equilibrium modeling, we obtained the compositions and proportions of minerals and melt for various temperatures, pressures, and water contents. To estimate the trace element composition of the melt, we employed the batch (equilibrium) melting equation (Shaw, 1970): $C_{melt}/C_{source} = 1/[D + F\times(1–D)]$, where C_{source} and C_{melt} denote the concentration of trace elements in the source and the melt, respectively, F represents the melt percentage, and D is the bulk partition coefficient: $D = x_1Kd_1 + x_2Kd_2 + x_3Kd_3$ …, where Kd is the mineral/melt partition coefficient and x_i refers to the mass fraction of a particular mineral out of the total crystallized assemblages (Supplementary Table 8).

3.2. Magmatic fO_2 and H_2O calculation

Based on thermodynamic considerations and empirical calibration, Loucks et al. (2020) proposed an independent oxybarometer based on Ce, U and Ti contents (ppm) in zircon: $\Delta FMQ = 3.998\ (\pm 0.124)\ \log[Ce/\sqrt{U_i \times Ti}] + 0.2284\ (\pm 0.101)$, in which ΔFMQ is magmatic fO_2 relative to the FMQ buffer and U_i is initial U corrected for radioactive decay. For H_2O content, we employed a recently developed zircon-based oxybarometer-hygrometer as detailed in Ge et al., 2023. This innovative method requires input of zircon trace elements, oxygen fugacity (fO_2) values, as well as whole-rock major and trace element compositions. Calculations are performed through an electronic spreadsheet.

Comprehensive methodology and additional information are available in Ge et al., 2023.

The zircon U-Pb dating and trace elements analysis were acquired using a Cameca IMS-1300HR SIMS at Nanjing University. Detailed analytical methods are available in Supplementary information.

3.3. Proxies used to filter altered zircon

Early Earth zircons are susceptible to radiation damage, often showing significant alpha-dose accumulation leading to amorphization even at moderate actinide contents (Bell et al., 2016). Radiation-damaged zircons, being porous and fractured, are particularly sensitive to fluid-induced chemical modifications. This results in enrichment of light rare earth elements (LREEs), calcium (Ca), and iron (Fe), or their replacement by secondary alteration products (Kitajima et al., 2012). Several chemical alteration proxies were used to identify altered zircons in this study. (1) The Light Rare Earth Element Index (LREE-I): Following Bell et al. (2016), this index is calculated as (Dy/Nd) + (Dy/Sm). A threshold value of LREE-I > 30 was used to identify pristine zircons. (2) Lanthanum (La) concentrations: La shows the most significant modification during post-magmatic alteration among the REEs. Pristine zircons have La concentrations normalized to C1 chondrite (La_N) < 1 (Zeh et al., 2014). This threshold was relaxed to <2 in this study to account for the often substantial uncertainties in La measurements. (3) Calcium and iron concentrations: A maximum limit of 150 ppm was set for both Ca and Fe concentrations to identify pristine zircons (Kitajima et al., 2012). (4) U-Pb isotopic data: Pristine zircons were commonly identified by a degree of discordance <5 % and a fraction of non-radiogenic Pb < 1 % (Zeh et al., 2014).

4. Results and discussion

4.1. fO_2 and H_2O of Paleo- to Meso- Archean granitoid rocks

Magmatic oxygen fugacity (fO_2) and water content (H_2O) are pivotal factors influencing magma formation, differentiation, and metallogenic

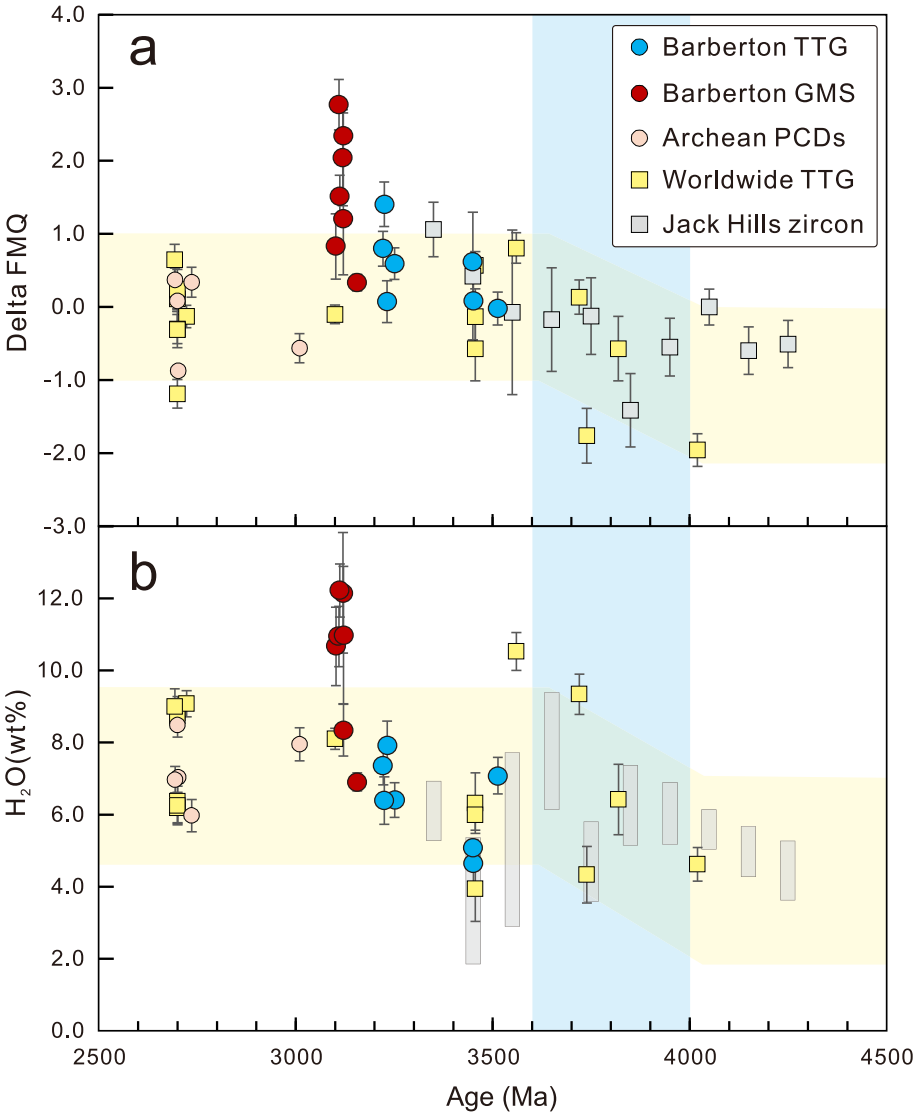

Fig. 2. The secular variations of magmatic oxygen fugacity and water content of granitoid rocks from Hadean to Archean. (a) Variation of magmatic oxygen fugacity (fO_2) of granitoid rocks with age, each symbol represent median ± 2 s.e., same as in b. In addition, fO_2 of Archean porphyry deposits (PCDs) are also plotted. (b) Variation of magmatic water content (H_2O) of granitoid rocks, which shows a similar trend with magmatic fO_2. The grey rectangles show the ranges of model H_2O contents for the Jack Hills zircons calculated assuming source compositions (Ge et al., 2023). The blue shaded time window (4.0–3.6 Ga) of increasing magmatic fO_2 and H_2O contents indicate the onset of subduction and deep-water recycling (Ge et al., 2023). Data on worldwide TTG, PCDs, and Jack Hills zircons are complied from literatures (Supplementary Table 3). (For interpretation of the references to colour in this figure legend, the reader is referred to the web version of this article.)

processes (Kelley and Cottrell, 2009; Zimmer et al., 2010), and they exhibit distinct characteristics across different tectonic settings. In subduction zones, arc magmas typically display elevated fO_2 and H_2O contents due to the infiltration of oxidizing fluids from the subducting oceanic crust into the mantle wedge (Kelley and Cottrell, 2009; Lee et al., 2010; Zimmer et al., 2010; Gao et al., 2022). By contrast, magmas in intraplate settings generally have low fO_2 and H_2O contents, reflecting the relatively dry and reduced environments of the Earth's deep mantle (Berry et al., 2008; Cottrell et al., 2021). Therefore, examining the fO_2 values and H_2O contents of Archean granitoids provides critical insights into the tectonic processes on the early Earth.

In this study, we present 362 in-situ trace-element and 145 in situ U-Pb dating analyses for magmatic zircons of ca. 3.51–3.22 Ga TTGs and ca. 3.11–3.10 Ga potassic granites from the eastern Kaapvaal craton (Supplementary Table 1 and 2; Fig. S1). A recently developed zircon-based oxybarometer-hygrometer (Ge et al., 2023; Loucks et al., 2020) was used to estimate the fO_2 values and H_2O contents. The results indicate that the ca. 3.51 Ga TTGs exhibit magmatic fO_2 within 1 log unit of the fayalite–magnetite–quartz (FMQ) buffer (median FMQ −0.02 ± 0.2, 2 standard error (2 s.e.), which are used throughout the text), whereas the two ca. 3.45 Ga TTG plutons show a median ΔFMQ of +0.09 ± 0.31 and + 0.62 ± 0.1. Moving forward in time, the ca. 3.25 Ga TTGs display a median ΔFMQ of +0.59 ± 0.2, and the subsequent ca. 3.22 Ga TTGs exhibit a broader range with ΔFMQ ranging from +0.07 ± 0.3 to +1.4 ± 0.3 (Fig. 2a). In contrast, the ca. 3.11–3.10 Ga GMS rocks display a wide variation in magmatic fO_2, with a median ΔFMQ spanning from +0.3 ± 0.1 to +2.7 ± 0.3 (Fig. 2a). Consistent with the fO_2 trends, the H_2O content shows a similar progression: the median H_2O content in the magmas decreases from 7.1 wt% at ca. 3.51 Ga, to 5.1 wt% around 3.45 Ga. It subsequently rises again to 6.0 wt% at about 3.25 Ga, and for the ca. 3.22 Ga samples, it spans a broader range from 6.4 to 7.9 wt% (Fig. 2b). The ca. 3.11–3.10 Ga GMS rocks have H_2O contents that significantly surpass the average of the ca. 3.51 to 3.22 Ga TTGs, exhibiting a broad span from 6.9 to 12.2 wt% (Fig. 2b).

To provide a comparative perspective, we plotted the fO_2 and H_2O contents of ca. 4.0–2.7 Ga old TTGs from different cratons, of ca. 4.3–3.4 Ga Jack Hills zircon, binned in 100-million-year intervals, and of ca. 3.0–2.7 Ga porphyry Cu-Au-Mo deposits (Fig. 2a,b; Supplementary Table 3). The observation of an overall increase in magmatic fO_2 and H_2O in granitoids during the Eoarchaean (4.0–3.6 Ga) has been interpreted as indicative of a shift from stagnant-lid to mobile-lid tectonics (Ge et al., 2023). This interpretation is supported by Ti and Si isotope studies that record the onset of recycling of hydrated crust (Aarons et al., 2020; Zhang et al., 2023) and is further corroborated by the positive shift in initial zircon Hf isotope compositions (Næraa et al., 2012; Bauer et al., 2020). While individual cratons have distinct evolutionary paths, linked to their regional tectonic histories, a common theme emerges in the progression from initially low magmatic fO_2 and H_2O concentrations toward higher values (Gao et al., 2022).

The BGGT exhibits a comparable trend between ca. 3.51 and 3.22 Ga, with a conspicuous peak in fO_2 for the TTGs around 3.22 Ga (median ΔFMQ of +1.4 ± 0.3), surpassing the mean value recorded in worldwide TTGs. The abrupt increase in fO_2 and H_2O content of TTGs in ca. 3.23–3.22 Ga (Fig. 2a,b) is consistent with increased $\delta^{18}O$ values of zircon and whole-rock Dy/Yb ratios (Fig. 4b; Wang et al., 2022), which indicate seawater hydrothermal alterated crust transported to depth and melting through subduction (Wang et al., 2022). Although the mechanism of subduction initiation remains debated, impact events have been proposed as a plausible trigger for promoting subduction, as supported by both numerical simulations (O'Neill et al., 2020) and terrestrial impact records in BGGT (Lowe, 2024). The subducted slab brings water and oxidized material to the depth (i.e., source region of TTG), similar to modern subduction zones, which feature water-rich and oxidized arc rocks (Kelley and Cottrell, 2009; Lee et al., 2010). With the advent of GMS rocks at ca. 3.11 Ga, both fO_2 and H_2O contents reached high values unprecedented in Archean era (Fig. 2a,b). The marked increase in magmatic fO_2 and H_2O contents, associated with the shift from TTGs to potassic granites in the eastern Kaapvaal craton, implies a potential shift in tectonic setting.

We further compared fO_2 and H_2O in Archean granitoids (including TTGs and GMS rocks) with basalts and granites of different ages from diverse tectonic environments (Fig. 3; Supplementary Table 3). During the Phanerozoic, there is a coherent increase in fO_2 and H_2O content from MORB, through arc basalts, culminating in the highest values in collision-related granites and Cu-Au deposits (Fig. 3). Arc magmas are characterized by elevated fO_2 values and H_2O contents, a consequence of the infiltration of oxidizing fluids from subducting oceanic crust (Kelley and Cottrell, 2009; Lee et al., 2010). As the tectonic setting shifts from subduction to collision, arc-related rocks are progressively incorporated into collisional process, signifying a transformation from crustal growth to reworking (Cawood et al., 2022). The collision-related granite and porphyry deposits show higher fO_2 values and H_2O contents, as observed in modern collisional belts (Fig. 3; Supplementary Table 3). For the Archean, a parallel trend emerges: MORB-like basalts exhibit the lowest values of fO_2, followed by a gradual increase through arc-like basalts and TTGs from diverse cratons, ultimately reaching peak values in ca. 3.11–3.10 Ga GMS rocks (Fig. 3). Considering the parallel trends, the ca. 3.11–3.10 Ga GMS rocks in the BGGT, with their notably high fO_2 and H_2O contents, are taken to reflect the horizontal tectonic thickening that might be driven by subduction between ca. 3.2 and 3.1 Ga. Experiments suggest that granitic magmas formed under high-pressure conditions exhibit higher water solubility (Baker and Alletti, 2012), which supports the hypothesis that GMS rocks formed in a thickened crustal setting.

A recent study posits that relatively oxidizing and wet magmas resembling Archean granitoids worldwide can result from melts derived from partial melting of an overthickened mafic crust in a non-subduction scenario (Hernández-Uribe, 2024), and these thermodynamic-based modeling results are also plotted in Fig. 3. The fO_2 values and H_2O contents of modeled melts cover the spectrum of Archean TTGs, indicating that subduction was not the only way for achieving such high fO_2 values and H_2O contents (Fig. 3). However, fO_2 values of the ca. 3.11–3.10 Ga GMS rocks are significantly higher, up to 1–2 orders of magnitude higher than those predicted by these modeled melts and Archean TTGs, and their H_2O contents are also higher, up to 10–14 wt% (Fig. 3; Supplementary Table 3). Endogenic oxidation by garnet retention/fractionation cannot explain the high fO_2 values and H_2O contents in these GMS rocks even if the melting depth was as deep as 40–45 km as suggested by Hernández-Uribe (2024). We therefore conclude that more oxidized and water-rich source components played a crucial role in the genesis of GMS rocks.

Overall, the trend for Archean rocks falls below that of Phanerozoic rocks in terms of fO_2 and H_2O contents (Fig. 3). Possible explanations include that slabs in the Archean subducted to shallower depths than in the Phanerozoic and were more prone to break-off due to higher mantle temperatures (Herzberg et al., 2010; Van Hunen and Moyen, 2012). As a result, this short-lived subduction has limited time to transport a large volume of water or oxidized material into deep source areas. Furthermore, the nature of the subducted seafloor material during the early Archean, particularly around the proposed onset of tectonics at ~3.2 Ga, may have differed significantly from modern analogues (Cawood et al., 2022; Ge et al., 2023). Rather than typical oceanic crust formed through seafloor spreading, the earliest subducted material might have been dominated by thick, volcanic plateau-like sequences formed through flood volcanism or similar processes (Byerly et al., 2019; Lowe, 2024). Such primitive oceanic crust would likely have been thicker and compositionally distinct, potentially affecting its alteration process and water content (Roman and Arndt, 2020). Additionally, the sedimentary cover on such crust was likely minimal and compositionally atypical—possibly including more mafic or chemically precipitated sediments rather than the oxidized terrigenous sediments common in later times (Lyons et al., 2014). Collectively, these factors would have

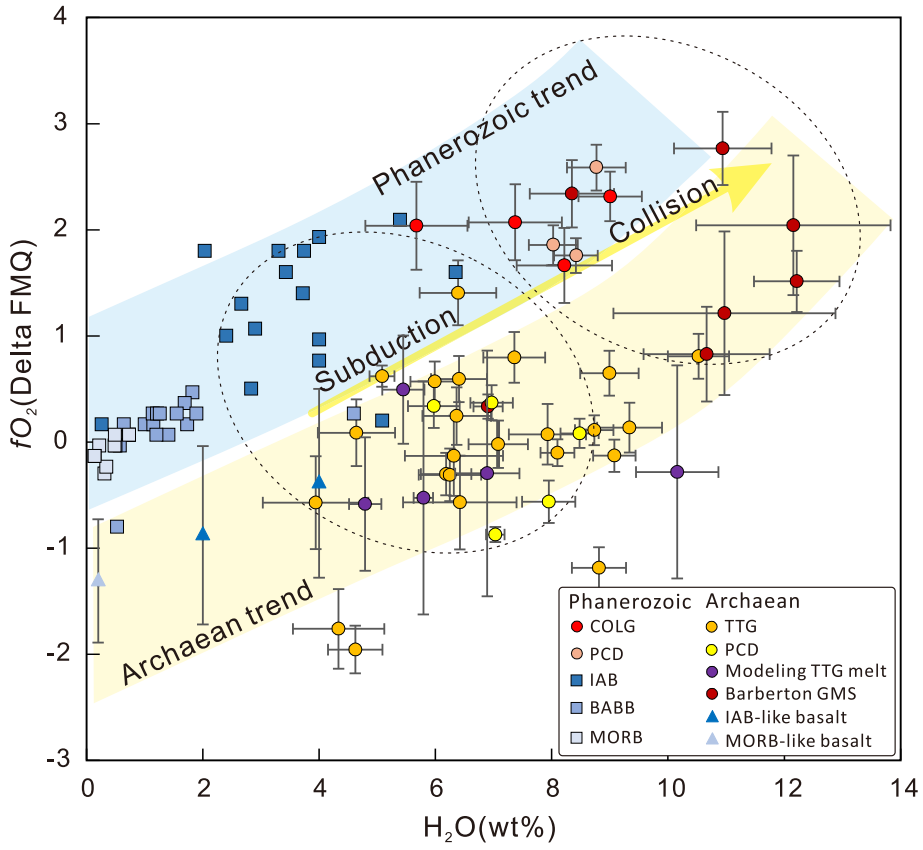

Fig. 3. fO_2 versus H_2O content of different tectonic settings and times. The melt inclusion data (square symbol) for Phanerozoic mid-ocean ridge basalt (MORB), back-arc basin basalt (BABB), island arc basalt (IAB) (Kelley and Cottrell, 2009; Zimmer et al., 2010), as well as fO_2 of MORB-like and IAB-like Archean basalts estimated using V/Ti ratios (triangle symbol) (Gao et al., 2022), are shown for comparison. In addition, fO_2 of Archean and Phanerozoic collision-related porphyry Cu ± Au ± Mo deposits (PCDs) and collision granite (COLG), calculated by zircon oxybarometer-hygrometer (circle symbol) are also plotted (data and cited literatures in Supplementary Table 3). Data of TTG melt modeling are given by Hernández-Uribe, 2024, and other data are complied from Ge et al., 2023. Each symbol represent the median, and error bars are 2 s.e.m. for the zircon oxybarometer-hygrometer results, 10 % for H_2O content and 0.25 log units for fO_2 for Phanerozoic melt inclusion data, and 1 s.d. for fO_2 of Archaean basalts.

lowered the fO_2 of fluids and melts released during subduction, thereby imposing a first-order control on the redox state of associated magmas (Fig. 3).

Variations in mantle oxygen fugacity may influence geochemical properties of crustal materials, a topic that has been extensively debated in recent years (Aulbach and Stagno, 2016; Nicklas et al., 2018, 2019; O'Neill and Aulbach, 2022). In particular, the rise in upper mantle fO_2 at the end of Archean has been attributed to the entrainment of perovskite from the deep mantle (O'Neill and Aulbach, 2022). This secular oxidation likely influenced the mantle source of arc volcanics, contributing to the observed shift in fO_2 of magmatic rocks over time. The gradually increasing mantle oxygen fugacity is also considered a potential factor in the occurrence of the Great Oxidation Event (Nicklas et al., 2019; O'Neill and Aulbach, 2022). However, the specific mechanisms through which this deep redox evolution affected shallow crustal oxidation processes—particularly in subduction zone settings—require further investigation.

4.2. Constraint from isotopes, thermodynamic and geochemical modeling

Earth's primordial cratons emerged through the recycling of Hadean to early Eoarchean crust (>3.80 Ga) by the addition of isotopically juvenile mantle-derived melts (Cawood et al., 2022). These processes are recorded in Hf isotope systematics as bimodal signatures (Hawkesworth et al., 2017; Cawood et al., 2022): suprachondritic values (reflecting mantle-derived inputs) and subchondritic values (indicative of crustal reworking). During later evolution, remelting of pre-existing continental crust—manifested by widespread potassic granite generation—drove a transition toward increasingly subchondritic isotopic compositions (Moyen et al., 2021; Rollinson et al., 2024). This diachronous shift across different cratons highlights their unique geodynamic histories (Cawood et al., 2022).

The eastern Kaapvaal craton records a multi-stage crustal evolution history between ca. 3.66 and 2.60 Ga, recorded by Lu-Hf and O isotope variations (Fig. 4a,b; Supplementary Table 4 and 5). Three temporally distinct periods are identified: (1) Primary crustal growth (ca. 3.66–3.40 Ga): supra-chondritic $\varepsilon_{Hf}(t)$ values (0 to +4.0) and mantle-like zircon $\delta^{18}O$ values (5.0–6.5 ‰) dominate this period (Fig. 4a,b), indicating derivation from a depleted mantle source with limited crustal contamination. (2) Transitional growth-reworking (ca. 3.28–3.22 Ga): this interval exhibits mixed isotopic signatures (Fig. 4a), including juvenile εHf(t) values (0 to +3.8) and moderately crustal-influenced $\varepsilon_{Hf}(t)$ values (−3.2 to 0). A pronounced shift is observed at ca. 3.22 Ga (Fig. 4b), marked by elevated zircon $\delta^{18}O$ (6.5–7.5 ‰) and increased TTG whole-rock Dy/Yb ratios (>2.5; Wang et al., 2022). These features suggest the involvement of supracrustal materials in magma generation at depths >40 km, potentially facilitated by proto-subduction processes (Wang et al., 2022), implying a tectonic shift toward crustal thickening or underthrusting. (3) Mature crustal reworking (ca. 3.11–2.60 Ga): subchondritic $\varepsilon_{Hf}(t)$ values (−12 to +1) prevail (Fig. 4a), reflecting extensive recycling of pre-existing continental crust.

The ca. 3.11–3.10 Ga GMS in BGGT primarily signifies a continental reworking period, as indicated by their sub-chondritic zircon $\varepsilon_{Hf}(t)$ values (Fig. 4a). To constrain the genesis of GMS rocks, three assumed

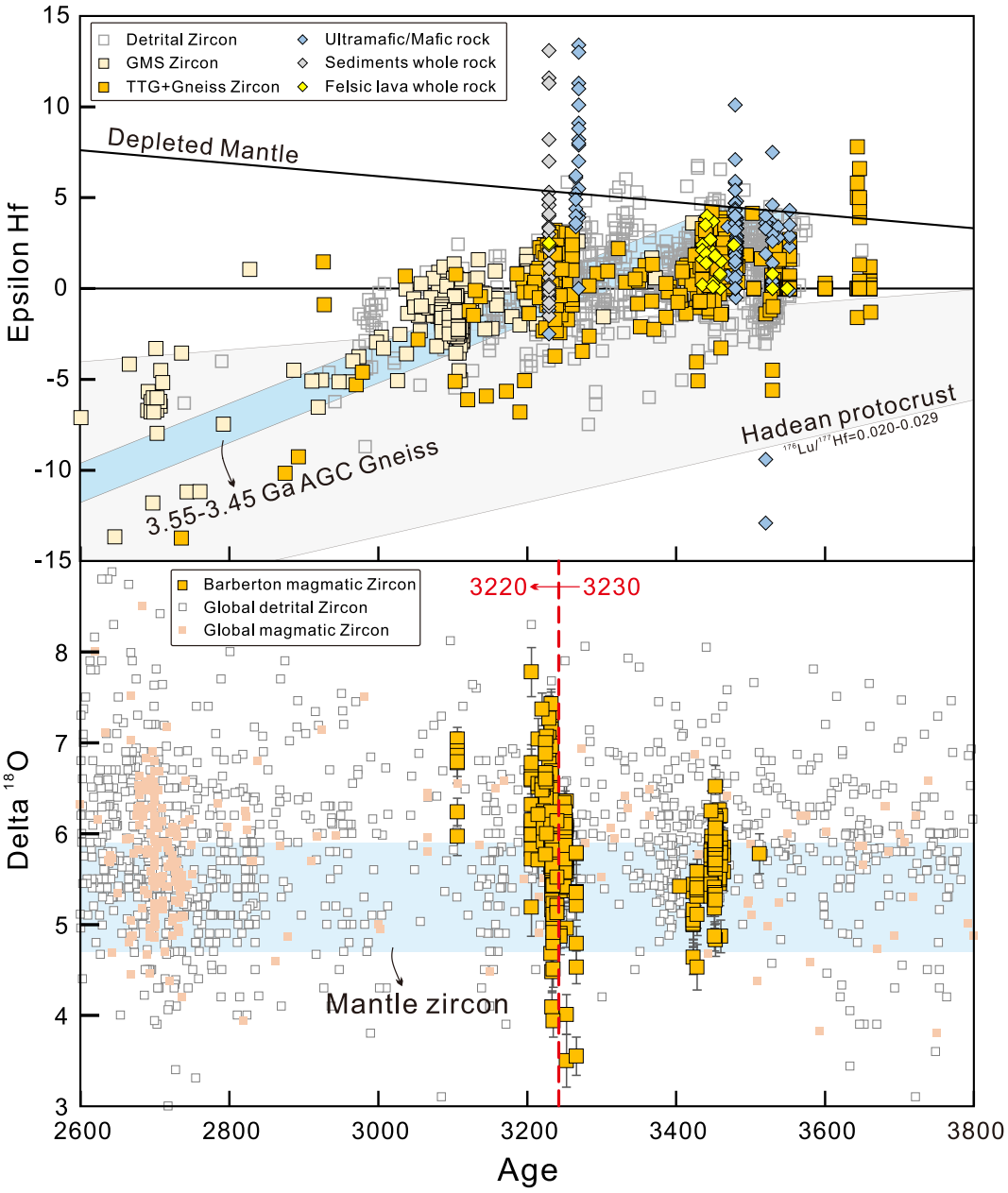

Fig. 4. Variation of Hf and O isotope data of BGGT and AGC with time. (a) Zircon and whole-rock Hf isotope data from different geological units of the BGGT and AGC; two evolutionary arrays are plotted: Hadean protocrust (light grey shadow) and AGC gneiss (light blue shadow). Each symbol represents one mineral or whole rock of one sample. (b) O isotope data of the BGGT magmatic zircons, global magmatic and detrital zircons. Each symbol represent median ± 2 s.e. Hf and O isotope data are complied from literatures (Supplementary Table 4 and 5). (For interpretation of the references to colour in this figure legend, the reader is referred to the web version of this article.)

sources have been proposed (Fig. 4a): (1) the ca. 3.55–3.45 Ga AGC grey gneisses, whose evolutionary domain encompasses a portion of sub-chondritic values, implying it could partly contribute to the formation of the GMS; (2) the ca. 3.51–3.22 Ga TTGs in BGGT; and (3) the ca. 3.2 Ga sedimentary rocks in the BGB (Fig. 4a).

The petrogenetic relationship between TTGs and GMS rocks remains a subject of ongoing investigation. While there is broad consensus that TTGs originate from partial melting of hydrated and silicified mafic crust (Moyen and Martin, 2012; Ding et al., 2024), the genesis of GMS rocks continues to present unresolved complexities (Moyen et al., 2021; Rollinson et al., 2024). Geochemical distinctions are particularly evident in the GMS suite, which exhibits marked potassium enrichment ($K_2O/Na_2O > 0.6$) compared to typical TTGs ($K_2O/Na_2O < 0.6$), along with 3–5 times higher concentrations of most trace elements (excluding Sr, Eu, and Ti) (Fig. S2; Supplementary Table 6). These characteristics suggest either derivation from a more evolved source or generation through a lower degree of partial melting (Moyen et al., 2021; Rollinson et al., 2024). To address these uncertainties, we conducted integrated thermodynamic-geochemical modeling of three potential source reservoirs (Fig. 5; Fig. S3; details in Methods; data in Supplementary Table 7 and 8).

Initial consideration of TTGs as potential precursors appears plausible given their crustal abundance and capacity to explain potassium enrichment through partial melting (Moyen and Martin, 2012; Rollinson et al., 2024). However, modeling results demonstrate fundamental incompatibilities, particularly regarding trace element concentration. Partial melts derived from TTGs in BGGT fail to replicate the enriched trace element contents observed in GMS rocks, with pronounced

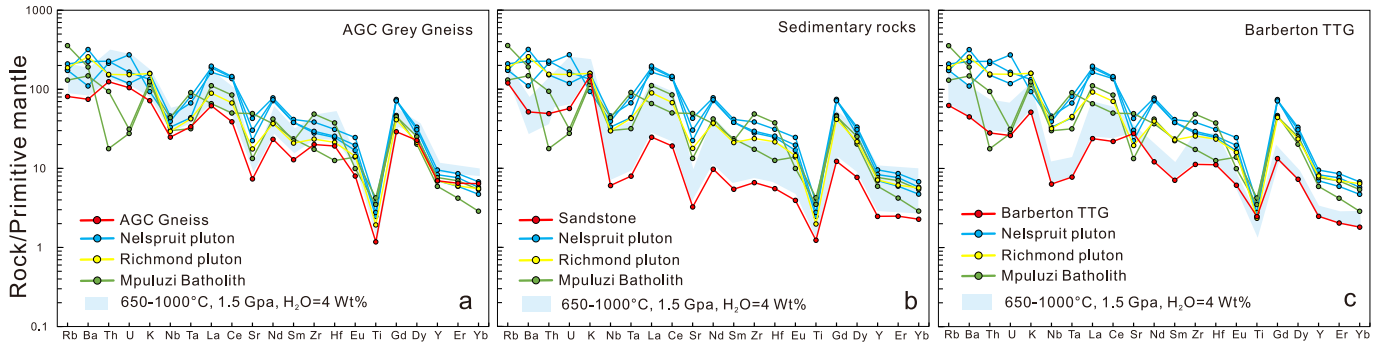

Fig. 5. Partial melting modeling of AGC grey gneiss (a), sedimentary rocks (b) and Barberton TTG (c). The coloured lines (except the red line) are 3.11–3.10 Ga GMS rocks. The blue shadows are modeled partial melts plotted for comparison. The pressure is set as 1.5 GPa, and modeling results for other pressure conditions are provided in Supplementary information. The initial water content is set as 4 wt%, considering the hornblende could be found in the Barberton TTGs. The data of AGC grey gneiss, sedimentary rocks and Barberton TTG were complied from literatures (more details in Methods section). (For interpretation of the references to colour in this figure legend, the reader is referred to the web version of this article.)

discrepancies in heavy rare earth element (HREE) patterns (Fig. 5c; Fig. S3). This mismatch likely reflects the inherent HREE depletion in TTGs, a geochemical signature inherited from garnet-bearing residues in their deep-seated source regions (Moyen and Martin, 2012). Similarly, while ca. 3.2 Ga BGB metasediments exhibit compatible $\varepsilon_{Hf}(t)$ values (Fig. 4a), both their bulk trace element compositions and modeled partial melts show significant deviations from GMS characteristics (Fig. 5b, Fig. S3). The argument against sedimentary sources gains additional support from low Ge/Si ratios in GMS rocks, which contrast sharply with values typical of sedimentary-derived melts (André et al., 2022).

In contrast, combined thermodynamic and trace-elements modeling demonstrates that 20–40 % partial melting of AGC grey gneisses (ca. 3.55–3.45 Ga) successfully reproduces trace element signatures of the GMS suite (Fig. 5a, Fig. S3). These heterogeneous crustal units, comprising metamorphosed TTGs, volcanosedimentary sequences, and amphibolites (Moyen and Martin, 2012), provide a viable source due to their volumetric dominance in Archean mid- to lower crust (Kröner et al., 2014; Hoffmann et al., 2016) and inherent geochemical variability. Isotopic evidence further supports this model, with $\varepsilon_{Hf}(t)$ evolutionary trends showing continuity between AGC gneisses and GMS rocks (Fig. 4a). The combined geochemical and isotopic evidence thus strongly implicates AGC grey gneisses as the primary source for ca. 3.11–3.10 Ga GMS rocks (Fig. 4a; Fig. 5a, Fig. S3), with potassium enrichment likely facilitated by biotite breakdown during gneiss melting and trace element enrichment achieved through moderate degree partial melting processes.

Although our trace element modeling and Hf isotopic constraints indicate that the grey gneiss of the AGC was the primary source of the GMS, we cannot exclude some contribution from more ancient Hadean/Eoarchean protocrust in the formation of these late-stage potassic rocks (Fig. 4a). According to Hf isotopic evolutionary trends, reworking of such ancient protocrust began around 3.6 Ga and continued until approximately 2.6 Ga (Fig. 4a; Zeh et al., 2014; Kröner et al., 2014). However, the extent and precise proportion of this protocrustal contribution to both the formation and reworking of the continental crust remain uncertain and warrant further investigation.

4.3. Magma crystallization depths in the eastern Kaapvaal craton

In transcrustal magmatic systems, magma derived from deep sources may experience multistage stagnation during ascent before ultimately consolidating at comparable depths (Annen et al., 2006; Bachmann and Huber, 2016). During the ascent of magma, continuously crystallizing minerals (e.g., zircon) record a series of pressure variations, which may correspond to the pressure differences as the magma moves from its source region to emplacement and consolidation (Brown, 1994; Moreira et al., 2023). Crucially, the final crystallization depth of magmatic systems is fundamentally governed by regional crustal thickness (Vigneresse et al., 1999; Loucks, 2021). In compressional tectonic settings, crustal thickening (>40 km) not only drives deeper partial melting (e.g., eclogite-facies depths >60 km) but also suppresses magma ascent through enhanced lithospheric viscosity, resulting in deep-seated crystallization (15–25 km). Conversely, in extensional settings, crustal thinning (<30 km) reduces melting temperatures and facilitates the formation of stable shallow magma chambers at 5–10 km depths (Vigneresse et al., 1999; Loucks, 2021). This tectono-depth coupling is globally validated by zircon-bearing magmas: plutons during supercontinent amalgamation (e.g., Rodinia) exhibit ~25 km average emplacement depths, approximately 12 km deeper than those (~8 km) during breakup stage (Moreira et al., 2023).

Here, we employ zircon $^{176}Lu/^{177}Hf$ barometry to constrain magma crystallization depths of ca. 3.51–3.10 Ga granitoid plutons in the BGGT and AGC (Moreira et al., 2023, Supplementary Table 4). The results show that the depths of TTG magma crystallization gradually increase from ca. 3.51 to 3.23 Ga, and that from ca. 3.22 to 3.10 Ga, there was a marked increase in the crystallization depth of the granitic magmas from ~15 km to ~50 km, coinciding with the petrogenetic shift from TTGs to potassic granites (Fig. 6). Notably, four magmatic pulses (ca. 3.51, ca. 3.45, ca. 3.23–3.22, and ca. 3.11–3.10 Ga) display significant variability of inferred magma crystallization depths within each episode (Fig. 6). The maximum crystallization depth in each episode can be taken to reflect the upper limit of the depths at which the magmas were generated within the crust, a depth constrained by the crust's thickness at that time (Vigneresse et al., 1999; Loucks, 2021). Thus, from ca. 3.22 to 3.10 Ga, the marked increase in the maximum crystallization depth of magma is taken to indicate progressive crustal thickening during this period (Fig. 6).

The interpretation of crustal thickening from ca. 3.22 to 3.10 Ga is reinforced by independent crustal thickness estimates: (i) detrital zircon Eu/Eu* systematics (Tang et al., 2021), and (ii) granitoid La/Yb ratios tracking garnet stability in the residue (Profeta et al., 2015). Both proxies show congruent thickening trends (Fig. S4), with crustal thickness increasing from ~40 km at 3.51 Ga to >70 km by 3.10 Ga. Such extreme thickening likely records the onset of horizontal tectonics at ~3.2 Ga, as evidenced by: (a) coeval high-pressure granulite facies metamorphism (Moyen et al., 2006; Taylor et al., 2012), and (b) development of thrust-imbricated greenstone belts (De Wit et al., 1992). These processes collectively enhanced lithospheric rigidity, culminating in cratonic stabilization of the eastern Kaapvaal by 3.1 Ga (Fig. 7).

4.4. Implications for craton stabilization and surficial environments

The long-term stability of cratonic crust has been classically

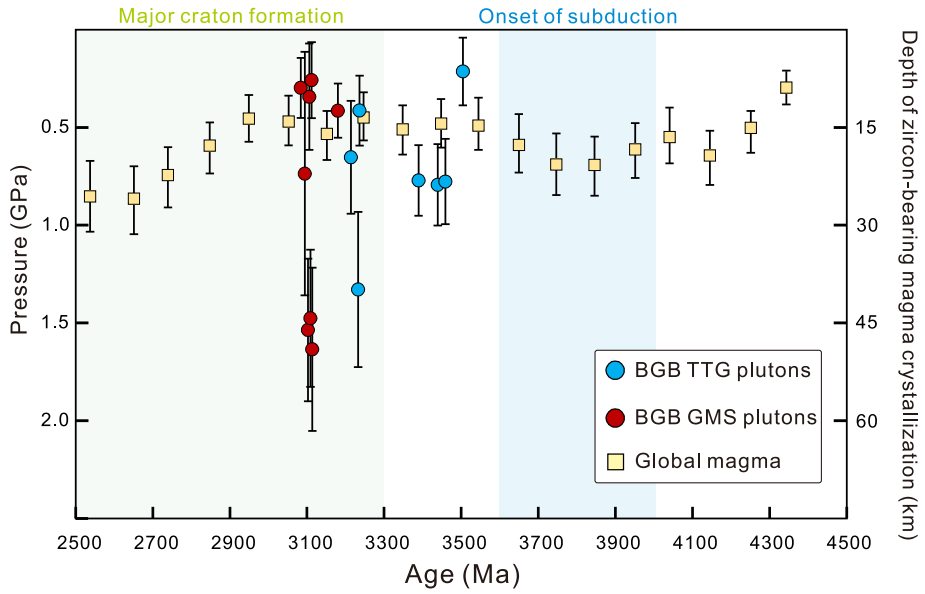

Fig. 6. Crystallization depth of granitic magma in the eastern Kaapvaal craton. Each blue circle represents a single TTG pluton in BGGT, and each red circle represents a sample from the GMS batholith. Each point is based on more than 10 analytical data, and represents median ± 2 s.e. The data highlight that the maximum depth of magma crystallization increased from ca. 3.51 to 3.10 Ga. The global data are time averaged data points from Moreira et al., 2023. (For interpretation of the references to colour in this figure legend, the reader is referred to the web version of this article.)

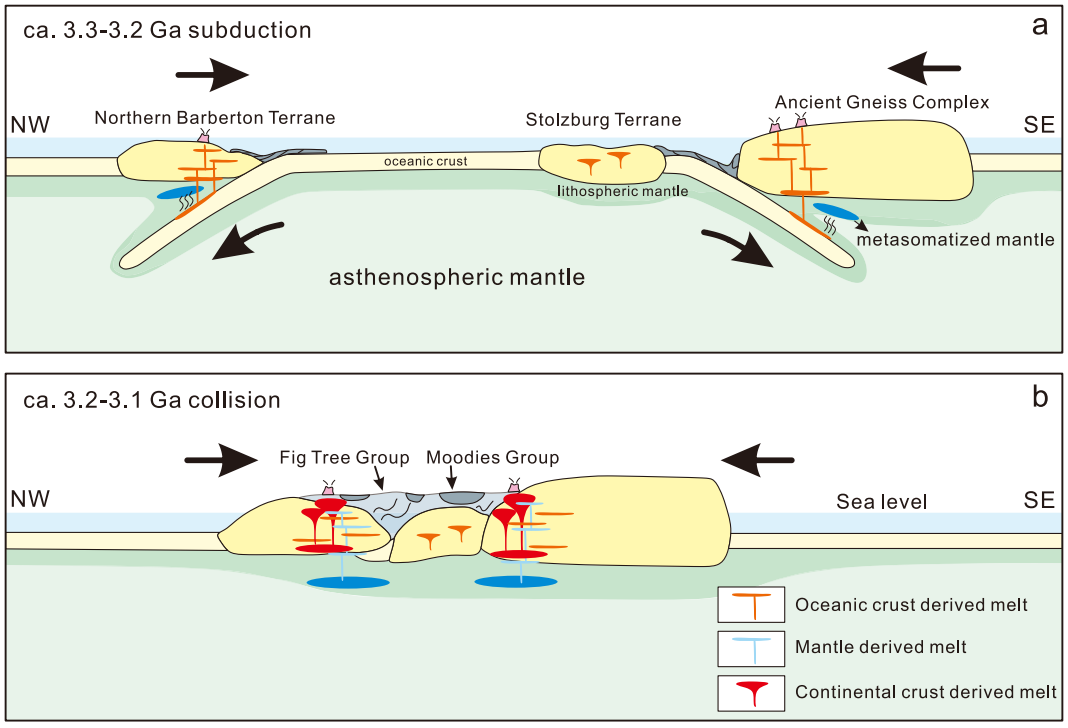

Fig. 7. Tectono-magmatic model for the eastern Kaapvaal Craton from approximately 3.3 to 3.1 Ga. (a) 3.3–3.2 Ga: Subducted slab transported supracrustal marterial to the deep area. Magmas from slab, lower and middle crust feature high-, middle-, and low-pressure characteristics. (b) 3.2–3.1 Ga: A massive volume of potassic granite are orginated from the grey gneiss of the lower continental crust during horizontal tectonic thickening. This figure is merely a conceptual illustration, so it could not provide precise boundaries of the tectonic plates.

attributed to the presence of a rigid lithospheric mantle root characterized by exceptional thickness, thermal deficit, anhydrous nature, and melt-depletion (Lee et al., 2011; Pearson et al., 2021). Although such chemically distinct thermal boundary layers exhibit prolonged isolation from the convecting mantle, their formation mechanisms remain controversial (Lee et al., 2011). While mantle plume models posit that high-temperature melting events generate dehydrated, depleted lithospheric keels (Griffin et al., 2003), this paradigm is difficult to reconcile with two key observations in the eastern Kaapvaal craton: (1) the systematic increase in magmatic oxygen fugacity (ΔFMQ 0.59–1.4 to 0.3–2.7) and water content (6.0–7.9 to 6.9–12.2 wt%) recorded in granitic magmas during 3.22–3.10 Ga (Fig. 2a,b); and (2) the concomitant deepening of magma crystallization depths as evidenced by zircon barometry (Fig. 6). These temporal correlations strongly suggest crustal

thickening through horizontal tectonic processes rather than vertical plume-driven mechanisms.

We propose that subduction-driven accretion during ca. 3.22–3.10 Ga initiated lithospheric stabilization through the following multi-stage process: First, the input of hydrated oceanic materials via slab subduction elevated deep oxidation states and fluid activity, accounting for the increase of magmatic fO_2, H_2O contents and $\delta^{18}O$ values (Fig. 2a,b; Fig. 4b). Second, lateral tectonic compression induced crustal shortening, explaining both the pressure estimates of coeval granulite-facies metamorphism (Moyen et al., 2006; Taylor et al., 2012) and the systematic increase in magma emplacement depths (Fig. 6). Third, crustal thickening promoted intracrustal differentiation, as demonstrated by the transition from ca. 3.66–3.22 Ga juvenile isotopic signatures to evolved crustal sources at ca. 3.11–3.10 Ga (Fig. 4a), particularly through remelting of pre-existing grey gneiss protoliths (Fig. 5). The protracted crustal evolution from 3.66 to 3.10 Ga progressively depleted the lithospheric mantle in heat-producing elements (HPEs; U, Th, K) through magmatic differentiation (Reimink and Smye, 2024). This geochemical depletion, combined with tectonic thickening, created a refractory mantle root resistant to remelting without external thermal input, ultimately establishing the craton's long-term stability (Liu et al., 2021).

From a geodynamic standpoint, the exceptional stability of Archean cratons is attributed to a unique, high-stress tectonic regime that was fundamentally different from modern plate tectonics. As proposed by Beall et al. (2018), their formation was not the product of persistent, Phanerozoic-style subduction but rather a catastrophic "lid-breaking" event during the transition from a stagnant-lid mantle convection mode to the onset of mobile-lid tectonics around 3 Ga. This episodic collapse of the stagnant lid generated transient, extreme compressional stresses (~150 MPa), far exceeding those in any subsequent tectonic regime. These stresses caused massive horizontal shortening and thrusting of buoyant, melt-depleted lithosphere, effectively stacking and amalgamating it into thick, stable cratonic nuclei. This mechanism explains why cratons formed almost exclusively in the Archean: post-Archean mantle cooling resulted in lower convective stresses (~75 MPa), preventing the recurrence of such extreme deformation events (Beall et al., 2018). Therefore, the episodic subduction-collision events suggested for the BGGT represent a manifestation of this brief, high-stress geodynamic threshold, which was critical for the irreversible stabilization of cratonic lithosphere.

The shift in tectonic processes in the eastern Kaapvaal craton during ca. 3.2–3.1 Ga appears to be linked to crustal thickening and cratonization (Fig. 7). The stabilization of felsic crust due to cratonization likely led to intense terrestrial weathering, and runoff transported essential nutrients, such as phosphorus, into the oceans, fueling the expansion of early life forms (Bindeman et al., 2018). Sediments from a more oxidized continent and increased population of oxygen-producing microbes in shallow coastal areas led to elevated levels of oxygen first in the shallow oceans and later in the atmosphere (Campbell and Davies, 2017). This link between continental emersion and the development of oxygenated environments is supported by several lines of evidence for shallow-marine oxygen oases as early as 3.0 Ga ago (Lyons et al., 2014; Eickmann et al., 2018). Additionally, the onset of widespread silicate weathering on the cratons is believed to have significantly reduced atmospheric CO_2 levels, facilitating a cooling effect and the onset of glacial periods, as suggested by the presence of Mesoarchean glacial diamictite formations (Hofmann and Bindeman, 2023). As more and more landmasses emerged from the oceans, alterations to Earth's surface environments became increasingly pronounced, enduring, and widespread, fundamentally reshaping the planet's habitability and climate dynamics (Bindeman et al., 2018).

5. Conclusions

(1) The eastern Kaapvaal craton underwent a tectonic transition from stagnant lid (3.66–3.23 Ga) to mobile lid (3.22–3.10 Ga) settings. This shift was recorded by marked increases in magmatic oxygen fugacity (fO_2), H_2O contents and $\delta^{18}O$ value from ca. 3.51–3.23 to 3.22–3.10 Ga. Concurrently, deeper magma crystallization depths and crustal thickness peaked at 3.11–3.10 Ga, reflecting horizontal tectonic thickening.
(2) Thermodynamic and geochemical modeling indicates that the ca. 3.11–3.10 Ga potassic granites formed by partial melting of the middle to lower crust (AGC gneiss) in regions of crustal thickening. This is also supported by isotopic shifts from juvenile to evolved Hf-O signatures.
(3) The Kaapvaal craton exemplifies how tectonic thickening during early mobile lid settings drove crustal maturation and craton stablization. This study highlights that tectonic transitions were critical in establishing the stability of Earth's earliest continents.

CRediT authorship contribution statement

All the co-authors have been involved in the work and agreed to its submission. **Ning Ding** initiated the idea, performed the experiments, collected data, conducted modeling, wrote the manuscript. **Chris J. Hawkesworth** initiated and developed the idea, wrote the manuscript. **Xiao-Lei Wang** designed the project, collected samples and wrote the manuscript. **Rong-Feng Ge** wrote the manuscript and contributed to the development of ideas. **Axel Hofmann** wrote the manuscript and contributed to field work. **Jun-Yong Li** wrote the manuscript and contributed to field work.

Declaration of competing interest

The authors declare that they have no known competing financial interests or personal relationships that could have appeared to influence the work reported in this paper.

Acknowledgements

We extend our gratitude to Craig O'Neill and Elis Hoffmann for their constructive comments, and to Marco Fiorentini for efficient editorial handling. This work was financially supported by the National Natural Science Foundation of China (No. 42025202), the "GeoX" interdisciplinary research funds for the Frontiers Science Center for Critical Earth Material Cycling (No. 2024JC03), the Fundamental Research Funds for the Central Universities of Ministry of Education (0206-14380176), and the State Key Laboratory for Critical Earth Material Cycling and Mineral Deposits. We thank Yue Guan and Lan-lan Tian for SIMS zircon analysis.

Appendix A. Supplementary data

Supplementary data to this article can be found online at https://doi.org/10.1016/j.chemgeo.2025.123093.

Data availability

The data have been supplemented and are available on request.

References

Aarons, S.M., Reimink, J.R., Greber, N.D., Heard, A.W., Zhang, Z., Dauphas, N., 2020. Titanium isotopes constrain a magmatic transition at the Hadean-Archean boundary in the Acasta Gneiss complex. Sci. Adv. 6, eabc9959. https://doi.org/10.1126/sciadv.abc9959.

André, L., Monin, L., Hofmann, A., 2022. The origin of early continental crust: New clues from coupling Ge/Si ratios with silicon isotopes. Earth Planet. Sci. Lett. 582, 117415. https://doi.org/10.1016/j.epsl.2022.117415.

Annen, C., Blundy, J.D., Sparks, R.S.J., 2006. The genesis of intermediate and silicic magmas in Deep Crustal Hot zones. J. Petrol. 47, 505–539. https://doi.org/10.1093/petrology/egi084.
Armstrong, R.A., Compston, W., De Wit, M.J., Williams, I.S., 1990. The stratigraphy of the 3.5-3.2 Ga Barberton Greenstone Belt revisited: a single zircon ion microprobe study. Earth Planet. Sci. Lett. 101, 90–106. https://doi.org/10.1016/0012-821X(90)90127-J.
Aulbach, S., Stagno, V., 2016. Evidence for a reducing Archean ambient mantle and its effects on the carbon cycle. Geology 44, 751–754. https://doi.org/10.1130/G38070.1.
Bachmann, O., Huber, C., 2016. Silicic magma reservoirs in the Earth's crust. Am. Mineral. 101, 2377–2404. https://doi.org/10.2138/am-2016-5675.
Baker, D.R., Alletti, M., 2012. Fluid saturation and volatile partitioning between melts and hydrous fluids in crustal magmatic systems: the contribution of experimental measurements and solubility models. Earth Sci. Rev. 114, 298–324. https://doi.org/10.1016/j.earscirev.2012.06.005.
Bauer, A.B., Reimink, J.R., Chacko, T., Foley, B.J., Shirey, S.B., Pearson, D.G., 2020. Hafnium isotopes in zircons document the gradual onset of mobile-lid tectonics. Geochem. Persp. Let. 14, 1–6. https://doi.org/10.7185/geochemlet.2015.
Beall, A.P., Moresi, L., Cooper, C.M., 2018. Formation of cratonic lithosphere during the initiation of plate tectonics. Geology 46, 487–490. https://doi.org/10.1130/G39943.1.
Bell, E.A., Boehnke, P., Harrison, T.M., 2016. Recovering the primary geochemistry of Jack Hills zircons through quantitative estimates of chemical alteration. Geochim. Cosmochim. Acta 191, 187–202. https://doi.org/10.1007/s00410-016-1236-x.
Berry, A.J., Danyushevsky, L.V., O'Neill, H.S.C., Newville, M., Sutton, S.R., 2008. Oxidation state of iron in komatiitic melt inclusions indicates hot Archaean mantle. Nature 455, 960–963. https://doi.org/10.1038/nature07377.
Bindeman, I.N., Zakharov, D.O., Palandri, J., Greber, N.D., Dauphas, N., Retallack, G.J., Hofmann, A., Lackey, J.S., Bekker, A., 2018. Rapid emergence of subaerial landmasses and onset of a modern hydrologic cycle 2.5 billion years ago. Nature 557, 545–548. https://doi.org/10.1038/s41586-018-0131-1.
Brown, M., 1994. The generation, segregation, ascent and emplacement of granite magma: the migmatite-to-crustally-derived granite connection in thickened orogens. Earth Sci. Rev. 36, 83–130. https://doi.org/10.1016/0012-8252(94)90009-4.
Byerly, G.R., Lowe, D.R., Heubeck, C., 2019. Geologic evolution of the barberton greenstone belt—a unique record of crustal development, surface processes, and early life 3.55–3.20 Ga. In: Earth's Oldest Rocks. Elsevier, pp. 569–613. https://doi.org/10.1016/B978-0-444-63901-1.00024-1.
Campbell, I.H., Davies, D.R., 2017. Raising the continental crust. Earth Planet. Sci. Lett. 460, 112–122. https://doi.org/10.1016/j.epsl.2016.12.011.
Cawood, P.A., Chowdhury, P., Mulder, J.A., Hawkesworth, C.J., Capitanio, F.A., Gunawardana, P.M., Nebel, O., 2022. Secular evolution of continents and the earth system. Rev. Geophys. 60, e2022RG000789. https://doi.org/10.1029/2022RG000789.
Connolly, J.A.D., 2009. The geodynamic equation of state: what and how. Geochem. Geophys. Geosyst. 10, Q10014. https://doi.org/10.1029/2009GC002540.
Cottrell, E., Birner, S.K., Brounce, M., Davis, F.A., Waters, L.E., Kelley, K.A., 2021. Oxygen fugacity across tectonic settings. Magma Redox Geochem. 33–61.
Cutts, K.A., Stevens, G., Hoffmann, J.E., Buick, I.S., Frei, D., Munker, C., 2014. Paleo- to Mesoarchean polymetamorphism in the Barberton Granite-Greenstone Belt, South Africa: Constraints from U-Pb monazite and Lu-Hf garnet geochronology on the tectonic processes that shaped the belt. Geol. Soc. Am. Bull. 126, 251–270. https://doi.org/10.1130/B30807.1.
De Wit, M.J., De Ronde, C.E.J., Tredoux, M., Roering, C., Hart, R.J., Armstrong, R.A., Green, R.W.E., Peberdy, E., Hart, R.A., 1992. Formation of an Archaean continent. Nature 357, 553–562. https://doi.org/10.1038/357553a0.
Dhuime, B., Wuestefeld, A., Hawkesworth, C.J., 2015. Emergence of modern continental crust about 3 billion years ago. Nat. Geosci. 8, 552–555. https://doi.org/10.1038/ngeo2466.
Ding, N., Wang, X.-L., Du, D.-H., Wang, D., Anhaeusser, C., 2024. Compositional diversity of TTGs controlled by heterogeneous accumulation of accessory minerals. Lithos 482–483, 107718. https://doi.org/10.1016/j.lithos.2024.107718.
Dziggel, A., Stevens, G., Poujol, M., Anhaeusser, C.R., Armstrong, R.A., 2002. Metamorphism of the granite–greenstone terrane south of the Barberton greenstone belt, South Africa: an insight into the tectono-thermal evolution of the 'lower' portions of the Onverwacht Group. Precambrian Res. 114, 221–247. https://doi.org/10.1016/S0301-9268(01)00225-X.
Eickmann, B., Hofmann, A., Wille, M., Bui, T.H., Wing, B.A., Schoenberg, R., 2018. Isotopic evidence for oxygenated Mesoarchaean shallow oceans. Nat. Geosci. 11, 133–138. https://doi.org/10.1038/s41561-017-0036-x.
Furnes, H., Dilek, Y., de Wit, M., 2015. Precambrian greenstone sequences represent different ophiolite types. Gondwana Res. 27, 649–685. https://doi.org/10.1016/j.gr.2013.06.004.
Gao, L., Liu, S.-W., Cawood, P.A., Hu, F.-Y., Wang, J.-T., Sun, G.-Z., Hu, Y.-L., 2022. Oxidation of Archean upper mantle caused by crustal recycling. Nat. Commun. 13, 3283. https://doi.org/10.1038/s41467-022-30886-4.
Ge, R.-F., Wlide, S., Zhu, W.-B., Wang, X.-L., 2023. Earth's early continental crust formed from wet and oxidizing arc magmas. Nature 623, 334–339. https://doi.org/10.1038/s41586-023-06552-0.
Griffin, W.L., O'Reilly, S.Y., Abe, N., Aulbach, S., Davies, R.M., Pearson, N.J., Doyle, B.J., Kivi, K., 2003. The origin and evolution of Archean lithospheric mantle. Precambrian Res. 127, 19–41. https://doi.org/10.1016/S0301-9268(03)00180-3.
Hawkesworth, C.J., Cawood, P.A., Dhuime, B., Kemp, T.I.S., 2017. Earth's continental lithosphere through time. Annu. Rev. Earth Planet. Sci. 45, 169–198. https://doi.org/10.1146/annurev-earth-063016-%20020525.
Hernández-Uribe, D., 2024. Generation of Archaean oxidizing and wet magmas from mafic crustal overthickening. Nat. Geosci. 17, 809–813. https://doi.org/10.1038/s41561-024-01489-z.
Herzberg, C., Condie, K., Korenaga, J., 2010. Thermal history of the Earth and its petrological expression. Earth Planet. Sci. Lett. 292, 79–88. https://doi.org/10.1016/j.epsl.2010.01.022.
Hoffmann, J.E., Kröner, A., 2019. Early archean crustal evolution in Southern Africa—an updated record of the ancient gneiss complex of Swaziland. In: Earth's Oldest Rocks. Elsevier, pp. 553–567. https://doi.org/10.1016/j.precamres.2016.01.026.
Hoffmann, J.E., Kröner, A., Hegner, E., Viehmann, S., Xie, H., Iaccheri, L.M., Schneider, K.P., Hofmann, A., Wong, J., Geng, H., Yang, J., 2016. Source composition, fractional crystallization and magma mixing processes in the 3.48–3.43Ga Tsawela tonalite suite (Ancient Gneiss complex, Swaziland) – Implications for Palaeoarchaean geodynamics. Precambrian Res. 276, 43–66. https://doi.org/10.1016/B978-0-444-63901-1.00007-1.
Hofmann, A., Bindeman, I.N., 2023. Earth's first glaciation at 2.9 Ga revealed by triple oxygen isotopes. Geochem. Persp. Let. 26, 20–24. https://doi.org/10.7185/geochemlet.2319.
Hofmann, A., Jodder, J., Xie, H., Bolhar, R., Whitehouse, M., Elburg, M., 2022. The Archaean geological history of the Singhbhum Craton, India–a proposal for a consistent framework of craton evolution. Earth Sci. Rev. 228, 103994. https://doi.org/10.1016/j.earscirev.2022.103994.
Holland, T.J.B., Powell, R., 2011. An improved and extended internally consistent thermodynamic dataset for phases of petrological interest, involving a new equation of state for solids. J. Metamorph. Geol. 29, 333–383. https://doi.org/10.1111/j.1525-1314.2010.00923.x.
Kamo, S.L., Davis, D.W., 1994. Reassessment of Archean crustal development in the Barberton Mountain Land, South Africa, based on U-Pb dating. Tectonics 13, 167–192. https://doi.org/10.1029/93TC02254.
Keller, C.B., Schoene, B., 2012. Statistical geochemistry reveals disruption in secular lithospheric evolution about 2.5 Gyr ago. Nature 485, 490–493. https://doi.org/10.1038/nature11024.
Kelley, K.A., Cottrell, E., 2009. Water and the Oxidation State of Subduction Zone Magmas. Science 325, 605–607. https://doi.org/10.1126/science.1174156.
Kisters, A.F.M., Anhaeusser, C.R., 1995. Emplacement features of Archaean TTG plutons along the southern margin of the Barberton greenstone belt, South Africa. Precambrian Res. 75, 1–15. https://doi.org/10.1016/0301-9268(95)00003-N.
Kitajima, K., Ushikubo, T., Kita, N.T., Maruyama, S., Valley, J.W., 2012. Relative retention of trace element and oxygen isotope ratios in zircon from Archean rhyolite, Panorama Formation, North Pole Dome, Pilbara Craton, Western Australia. Chem. Geol. 332–333, 102–115. https://doi.org/10.1016/j.chemgeo.2012.09.019.
Kröner, A., Hofmann, A. (Eds.), 2019. The Archaean Geology of the Kaapvaal Craton, Southern Africa, Regional Geology Reviews. Springer International Publishing, Cham.
Kröner, A., Hoffmann, J.E., Xie, H., Münker, C., Hegner, E., Wan, Y., Hofmann, A., Liu, D., Yang, J., 2014. Generation of early Archaean grey gneisses through melting of older crust in the eastern Kaapvaal craton, southern Africa. Precambrian Res. 255, 823–846. https://doi.org/10.1016/j.precamres.2014.07.017.
Kröner, A., Wong, J., Xie, H., 2018. The oldest granite clast in the Moodies conglomerate, Barberton greenstone belt, South Africa, and its likely origin. South Afr. J. Geol. 121, 43–50. https://doi.org/10.25131/sajg.121.0001.
Laurent, O., Martin, H., Moyen, J.F., Doucelance, R., 2014. The diversity and evolution of late-Archean granitoids: evidence for the onset of "modern-style" plate tectonics between 3.0 and 2.5Ga. Lithos 205, 208–235. https://doi.org/10.1016/j.lithos.2014.06.012.
Lee, C.-T.A., Luffi, P., Le Roux, V., Dasgupta, R., Albaréde, F., Leeman, W.P., 2010. The redox state of arc mantle using Zn/Fe systematics. Nature 468, 681–685. https://doi.org/10.1038/nature09617.
Lee, C.-T.A., Luffi, P., Chin, E.J., 2011. Building and destroying continental mantle. Annu. Rev. Earth Planet. Sci. 39, 59–90. https://doi.org/10.1146/annurev-earth-040610-133505.
Liu, J.-G., Pearson, D.G., Wang, L.-H., Mather, K.A., Kjarsgaard, B.A., Schaeffer, A.J., Irvine, G.J., Kopylova, M.G., Armstrong, J.P., 2021. Plume-driven recratonization of deep continental lithospheric mantle. Nature 592, 732–736. https://doi.org/10.1038/s41586-021-03395-5.
Loucks, R.R., 2021. Deep entrapment of buoyant magmas by orogenic tectonic stress: its role in producing continental crust, adakites, and porphyry copper deposits. Earth Sci. Rev. 220, 103744. https://doi.org/10.1016/j.earscirev.2021.103744.
Loucks, R.R., Fiorentini, M.L., Henríquez, G.J., 2020. New magmatic oxybarometer using trace elements in Zircon. J. Petrol. 61, egaa034. https://doi.org/10.1093/petrology/egaa034.
Lowe, D.R., 2024. Onverwacht group, barberton greenstone belt, South Africa: 300 m.y. development of a paleoarchean stagnant lid. Geol. Soc. Am. Bull. 137, 259–278. https://doi.org/10.1130/B37573.1.
Lyons, T.W., Reinhard, C.T., Planavsky, N.J., 2014. The rise of oxygen in Earth's early ocean and atmosphere. Nature 506, 307–315. https://doi.org/10.1038/nature13068.
Martin, H., Smithies, R.H., Rapp, R., Moyen, J.-F., Champion, D., 2005. An overview of adakite, tonalite–trondhjemite–granodiorite (TTG), and sanukitoid: relationships and some implications for crustal evolution. Lithos 79, 1–24. https://doi.org/10.1016/j.lithos.2004.04.048.
Moreira, H., Buzenchi, A., Hawkesworth, C.J., Dhuime, B., 2023. Plumbing the depths of magma crystallization using 176Lu/177Hf in zircon as a pressure proxy. Geology 51, 233–237. https://doi.org/10.1130/G50659.1.

Moser, D.E., Flowers, R.M., Hart, R.J., 2001. Birth of the Kaapvaal Tectosphere 3.08 billion years ago. Science 291, 465–468. https://doi.org/10.1126/science.291.5503.465.
Moyen, J.-F., Martin, H., 2012. Forty years of TTG research. Lithos 148, 312–336. https://doi.org/10.1016/j.lithos.2012.06.010.
Moyen, J.-F., Stevens, G., Kisters, A., 2006. Record of mid-Archaean subduction from metamorphism in the Barberton terrain, South Africa. Nature 442, 559–562. https://doi.org/10.1038/nature04972.
Moyen, J.-F., Stevens, G., Kisters, A.F.M., Belcher, R.W., Lemirre, B., 2019. TTG plutons of the barberton granitoid-greenstone terrain, South Africa. In: Earth's Oldest Rocks. Elsevier, pp. 615–653. https://doi.org/10.1016/B978-0-444-63901-1.00025-3.
Moyen, J.-F., Zeh, A., Cuney, M., Dziggel, A., Carrouée, S., 2021. The multiple ways of recycling Archaean crust: a case study from the ca. 3.1 Ga granitoids from the Barberton Greenstone Belt, South Africa. Precambrian Res. 353, 105998. https://doi.org/10.1016/j.precamres.2020.105998.
Næraa, T., Scherstén, A., Rosing, M.T., Kemp, A.I.S., Hoffmann, J.E., Kokfelt, T.F., Whitehouse, M.J., 2012. Hafnium isotope evidence for a transition in the dynamics of continental growth 3.2 Gyr ago. Nature 485, 627–630. https://doi.org/10.1038/nature11140.
Næraa, T., Kemp, A.I.S., Scherstén, A., Rehnström, E.F., Rosing, M.T., Whitehouse, M.J., 2014. A lower crustal mafic source for the ca. 2550 Ma Qôrqut Granite complex in southern West Greenland. Lithos 192–195, 291–304. https://doi.org/10.1016/j.lithos.2014.02.013.
Nicklas, R.W., Puchtel, I.S., Ash, R.D., 2018. Redox state of the Archean mantle: evidence from V partitioning in 3.5–2.4 Ga komatiites. Geochim. Cosmochim. Acta 222, 447–466. https://doi.org/10.1016/j.gca.2017.11.002.
Nicklas, R.W., Puchtel, I.S., Ash, R.D., Piccoli, P.M., Hanski, E., Nisbet, E.G., Waterton, P., Pearson, D.G., Anbar, A.D., 2019. Secular mantle oxidation across the Archean-Proterozoic boundary: evidence from V partitioning in komatiites and picrites. Geochim. Cosmochim. Acta 250, 49–75. https://doi.org/10.1016/j.gca.2019.01.037.
O'Neill, C., Aulbach, S., 2022. Destabilization of deep oxidized mantle drove the Great Oxidation Event. Sci. Adv. 8, eabg1626. https://doi.org/10.1126/sciadv.abg1626.
O'Neill, C., Marchi, S., Bottke, W., Fu, R., 2020. The role of impacts on Archaean tectonics. Geology 48, 174–178. https://doi.org/10.1130/G46533.1.
Pearson, D.G., Scott, J.M., Liu, J., Schaeffer, A., Wang, L.H., Van Hunen, J., Szilas, K., Chacko, T., Kelemen, P.B., 2021. Deep continental roots and cratons. Nature 596, 199–210. https://doi.org/10.1038/s41586-021-03600-5.
Profeta, L., Ducea, M.N., Chapman, J.B., Paterson, S.R., Gonzales, S.M.H., Kirsch, M., Petrescu, L., DeCelles, P.G., 2015. Quantifying crustal thickness over time in magmatic arcs. Sci. Rep. 5, 17786. https://doi.org/10.1038/srep17786.
Reimink, J.R., Smye, A.J., 2024. Subaerial weathering drove stabilization of continents. Nature 629, 609–615. https://doi.org/10.1038/s41586-024-07307-1.
Robb, L.J., Meyer, F.M., Hawkesworth, C.J., Gardiner, N.J., 2021. Petrogenesis of Archaean granites in the Barberton region of South Africa as a guide to early crustal evolution. South Afr. J. Geol. 124, 111–140. https://doi.org/10.25131/sajg.124.0021.
Rollinson, H., Chagondah, G., Hofmann, A., 2024. The late Archaean granite paradox: a case study from the Zimbabwe Craton. Precambrian Res. 410, 107491. https://doi.org/10.1016/j.precamres.2024.107491.
Roman, A., Arndt, N., 2020. Differentiated Archean oceanic crust: its thermal structure, mechanical stability and a test of the sagduction hypothesis. Geochim. Cosmochim. Acta 278, 65–77. https://doi.org/10.1016/j.gca.2019.07.009.
Sanchez-Garrido, C.J.M.G., Stevens, G., Armstrong, R.A., Moyen, J.-F., Martin, H., Doucelance, R., 2011. Diversity in Earth's early felsic crust: paleoarchean peraluminous granites of the Barberton Greenstone Belt. Geology 39, 963–966. https://doi.org/10.1130/G32193.1.
Schoene, B., Dudas, F.O.L., Bowring, S.A., De Wit, M., 2009. Sm-Nd isotopic mapping of lithospheric growth and stabilization in the eastern Kaapvaal craton. Terra Nova 21, 219–228. https://doi.org/10.1111/j.1365-3121.2009.00877.x.
Shaw, D.M., 1970. Trace element fractionation during anatexis. Geochim. Cosmochim. Acta 34, 237–243. https://doi.org/10.1016/0016-7037(70)90009-8.
Smithies, R.H., 2000. The Archaean tonaliteˆtrondhjemiteˆgranodiorite (TTG) series is not an analogue of Cenozoic adakite. Earth Planet. Sci. Lett. 128, 115–125. https://doi.org/10.1016/S0012-821X(00)00236-3.
Suhr, N., Hoffmann, J.E., Kröner, A., Schröder, S., 2015. Archaean granulite-facies paragneisses from Central Swaziland: inferences on Palaeoarchaean crustal reworking and a complex metamorphic history. J. Geol. Soc. Lond. 172, 139–152. https://doi.org/10.1144/jgs2014-007.
Tang, M., Ji, W.-Q., Chu, X., Wu, A., Chen, C., 2021. Reconstructing crustal thickness evolution from europium anomalies in detrital zircons. Geology 49, 76–80. https://doi.org/10.1130/G47745.1.
Taylor, J., Stevens, G., Buick, I.S., Lana, C., 2012. Successive midcrustal, high-grade metamorphic events provide insight into Mid-Archean mountain-building along the SE margin of the proto-Kaapvaal craton. Geol. Soc. Am. Bull. 124, 1191–1211. https://doi.org/10.1130/B30543.1.
Van Hunen, J., Moyen, J.-F., 2012. Archean subduction: fact or fiction? Annu. Rev. Earth Planet. Sci. 40, 195–219. https://doi.org/10.1146/annurev-earth-042711-105255.
Vigneresse, J.-L., Tikoff, B., Améglio, L., 1999. Modification of the regional stress field by magma intrusion and formation of tabular granitic plutons. Tectonophysics 302, 203–224. https://doi.org/10.1016/S0040-1951(98)00285-6.
Wang, X.-L., Tang, M., Moyen, J., Wang, D., Kröner, A., Hawkesworth, C., Xia, X.-P., Xie, H.-Q., Anhaeusser, C., Hofmann, A., Li, J.-Y., Li, L.-S., 2022. The onset of deep recycling of supracrustal materials at the Paleo-Mesoarchean boundary. Natl. Sci. Rev. 9, nwab136. https://doi.org/10.1093/nsr/nwab136.
Zeh, A., Stern, R.A., Gerdes, A., 2014. The oldest zircons of Africa—Their U–Pb–Hf–O isotope and trace element systematics, and implications for Hadean to Archean crust–mantle evolution. Precambrian Res. 241, 203–230. https://doi.org/10.1016/j.precamres.2013.11.006.
Zhang, Q., Zhao, L., Zhou, D., Nutman, A.P., Mitchell, R.N., Liu, Y., Li, Q.-L., Yu, H.-M., Fan, B., Spencer, C.J., Li, X.-H., 2023. No evidence of supracrustal recycling in Si-O isotopes of Earth's oldest rocks 4 Ga ago. Sci. Adv. 9, eadf0693. https://doi.org/10.1126/sciadv.adf0693.
Zimmer, M.M., Plank, T., Hauri, E.H., Yogodzinski, G.M., Stelling, P., Larsen, J., Singer, B., Jicha, B., Mandeville, C., Nye, C.J., 2010. The role of water in generating the calc-alkaline trend: new volatile data for aleutian magmas and a new tholeiitic index. J. Petrol. 51, 2411–2444. https://doi.org/10.1093/petrology/egq062.